JACS
JOURNAL OF THE AMERICAN CHEMICAL SOCIETY
pubs.acs.org/JACS
Article

Single-Electron Transfer Stabilizes Metastable Alane in a Bipyridine-Functionalized MOF Nanopore

Mohana Shivanna, Nicole A. Torquato, Sichi Li, Maxwell A. T. Marple, Joshua D. Sugar, Michael E. Foster, Ashlynn Berry, William V. Taylor, Nicholas A. Strange, Xiaoling Wang, Farid El Gabaly, Tieyan Chang, Yu Sheng Chen, Peter A. Sharma, John Lemmon, Bryce Sadtler, Brandon C. Wood, Mark D. Allendorf,* and Vitalie Stavila*

Cite This: J. Am. Chem. Soc. 2025, 147, 47398−47408

Read Online

ACCESS | Metrics & More | Article Recommendations | Supporting Information

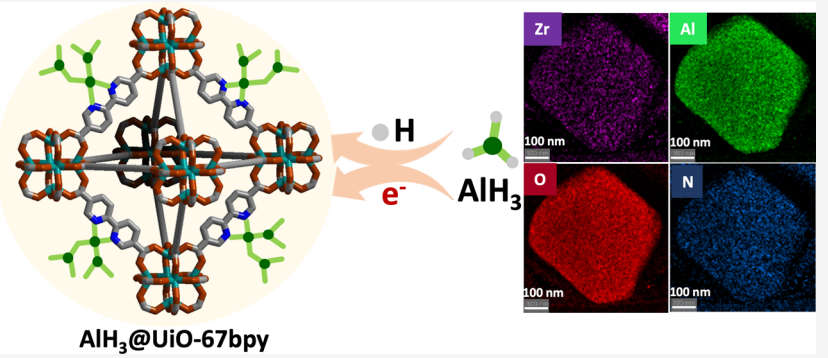

ABSTRACT: Nanoconfinement of metastable hydrides such as alane (AlH_3) in functionalized porous frameworks represents a promising yet largely untapped strategy for high-capacity energy storage. Despite its potential, the underlying mechanisms responsible for the thermodynamic stabilization of metastable hydrides are poorly understood. Here, concepts from solution Lewis acid−base chemistry were applied to a crystalline metal−organic framework (MOF) to stabilize AlH_3. The long-range order and synthetically versatile pore chemistry enabled us to reveal the intimate details of the hydride-host interactions. Powder X-ray diffraction (PXRD) of AlH_3-infiltrated UiO-67bpy ($Zr_6O_4(OH)_4(bpydc)_6$; $bpydc^{2-}$ = 2,2′-bipyridine-5,5′-dicarboxylate) confirms that the framework maintains its crystallinity up to 250 °C and is stable under 70 MPa H_2 pressure. We find that thermodynamic stabilization arises from coupled single-electron and hydrogen-atom transfer from AlH_3 to bipyridine-containing linkers. Electron paramagnetic resonance detects a bipyridyl radical with an anisotropic *g*-tensor (*g* values of 2.00132, 2.00215, and 2.00275), consistent with Bader charge analysis predicting 0.82 e^- transferred from the hydride to the MOF. These findings establish critical structure−property relationships underpinning AlH_3 stabilization and suggest general strategies for tuning the thermodynamics and kinetics of metastable materials.

INTRODUCTION

Metastable metal hydrides have long been of interest for hydrogen storage,[1] but also in applications requiring energy on demand,[2] as chemical reagents,[3] as superconductors,[4] and as an energetic material (*e.g.*, rocket fuel).[5] Among these, alane (AlH_3) has one of the highest gravimetric and volumetric energy storage capacities;[6] moreover, the dramatic expansion of hydrogen use cases under consideration makes AlH_3 even more attractive, as aluminum is an earth-abundant and low-cost element.[7] However, AlH_3 is metastable and usable under ambient conditions only by virtue of kinetic barriers to hydrogen release.[8,9] Calorimetry studies report values for the formation enthalpy of metastable AlH_3 ranging from −7.1 to −9.9 kJ/mol H_2,[10,11] making direct synthesis from the elements impractical due to the extreme hydrogen pressures required for the reaction (>25,000 bar[12]). Kinetic limitations exist as well, due to the native oxide layer on the Al surface.[5] Nevertheless, AlH_3 begins to decompose under mild temperatures (<100 °C) to form metallic aluminum and hydrogen, which is accelerated by the presence of trace amounts of transition metals, such as titanium.[9] Consequently, indirect and often complex preparation methods are necessary, such as reaction between $LiAlH_4$ and $AlCl_3$ in ethereal solutions,[8]

Received: September 10, 2025
Revised: November 19, 2025
Accepted: November 23, 2025
Published: December 10, 2025

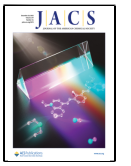

https://doi.org/10.1021/jacs.5c15894
J. Am. Chem. Soc. 2025, 147, 47398−47408

various electrochemical routes,[13] and stabilization by Lewis bases, particularly amines.[14]

An alternative approach is to use nanoconfinement within porous hosts to stabilize AlH_3. Nanoconfinement is a well-established strategy to accelerate hydrogen release from metal hydrides, which are typically quite thermally stable.[15] In contrast, we reasoned that nanoporous hosts with electron-donating capabilities would stabilize metastable hydrides due to synergistic effects of Lewis acid−base complex formation and inhibiting formation of bulk hydride agglomerates.[14,16] Analogous chemistry in solution[17] is the basis for two-step processes using amines and ethers to enable reversible hydrogen release from AlH_3.[14,18] We and others confirmed our hypothesis by coordinating $LiAlH_4$ to nitrogen-doped CMK-3,[19] hollow carbon spheres,[20] and by infiltrating a bipyridine-functionalized Covalent Triazine Framework with AlH_3 (AlH_3@CTF-bpy).[21] In all cases partial reversibility was observed. The behavior of AlH_3@CTF-bpy is particularly encouraging: rehydrogenation is achievable at 60 °C and 700 bar (35 times lower than required for bulk aluminum), with rapid H_2 desorption at temperatures as low as 150 °C. If this strategy is to be exploited for practical purposes, it is clear that the detailed nature of AlH_3 binding, the influence of pore size and electronic structure, and the mechanisms of hydrogen uptake and release must be understood so that desorption thermodynamics and kinetics can be tailored for specific applications while maximizing storage capacity. Unfortunately, both CTFs and porous carbons lack long-range order and have a distribution of pore sizes, making it difficult to confidently assign structure−property relationships. Although the thermodynamics of AlH_3 coordination to achieve hydrogen release under mild conditions have been quantified by electronic structure calculations,[14] the mechanism by which AlH_3 is stabilized within a nanopore and the nature of the confinement effects are not established.

Metal−organic frameworks (MOFs)[22,23] with their tailorable pore size and wide variety of pore chemical functionality, offer a solution to this problem. In particular, their crystallinity allows direct comparisons between first-principles atomic structure calculations and spectroscopic data. Our group has extensively explored the use of MOFs to create nanoscale hydrides, such as $NaAlH_4$ in MOF-74(Mg) and $Cu_3(btc)_2$ (btc^{3-} = 1,3,5-benzenetricarboxylate).[24,25] This work demonstrated that MOFs can be stable in the presence of chemically reducing metal hydrides and that nanoconfinement can change their chemical reactivity. Bipyridine-functionalized MOFs provide analogues to the CTFs used previously and have a high density of Lewis base groups[26] to coordinate to electron-deficient metal hydrides.[16] For example, we infiltrated UiO-67bpy to create "molecular" $Mg(BH_4)_2$ within the MOF pores. Recently, a number of other examples of metal hydrides hosted in MOFs have been reported.[27,28] For example, zirconium-based frameworks were recently used as hosts for metastable ammonia borane and hydrazine bis(borane).[29] In these cases, however, the guest species immediately released H_2 upon nanoconfinement by reacting with hydroxyl groups from the metal cluster, leading to the formation of (irreversible) B−O bonds. Many other MOFs are suitable for hosting various electron withdrawing guest species inside the framework, which can significantly alter their properties.[15,30]

Here, we demonstrate that the structural and electronic properties of the Lewis base functionalities within a MOF pore determine whether H_2 release from nanoconfined AlH_3 is reversible. Specifically, we hypothesize that an aromatic, chelating amine, such as bipyridine, is essential for reversibility. We demonstrate this using two MOFs: zirconium-based UiO-67 (biphenyldicarboxlyate linkers) and UiO-67bpy ($Zr_6O_4(OH)_4(bpydc)_6$; $bpydc^{2-}$ = 2,2′-bipyridine-5,5′-dicarboxylate); and two aliphatic compounds containing tertiary alkyl amines, cyclam and a G2 PPI dendrimer, serving as control systems. Our results show that formation of a stable aromatic amine radical occurs when AlH_3 coordinates within UiO-67bpy. This agrees with our previous observations of AlH_3 binding in CTFs.[21] AlH_3 incorporated within the pores of UiO-67bpy is thermodynamically stabilized and exhibits partial reversibility. In contrast, AlH_3 infiltrated within UiO-67 $Zr_6O_4(OH)_4(bpdc)_6$ ($bpdc^{2-}$ = biphenyldicarboxylate) releases hydrogen, but shows no rehydrogenation. Moreover, AlH_3 coordinated to the cyclam and dendrimer exhibits no rehydrogenation, confirming that strong Lewis base character alone is insufficient. Although a direct determination of the crystal structure of the confined AlH_3 clusters was not feasible due to severe disorder, extensive analytical data indicate that small Al-hydride clusters exist within the pores. This work firmly establishes a structure−property relationship, supported by experimental and first-principles modeling, that is grounded in a suite of six different AlH_3-incorporated materials. It also provides a second example of a porous framework thermodynamic stabilization initiated by single-electron transfer, showing that AlH_3@CTF-bpy is not unique in this regard.

RESULTS

Synthesis and Characterization. Synthesis of $Zr_6O_4(OH)_4(bpydc)_6$ or UiO-67bpy ($bpydc^{2-}$ = 2,2′-bipyridine-5,5′-dicarboxylate)[31] (see the Supporting Information for details) yielded colorless octahedron-shaped single crystals up to 20 μm as shown in Figure S1a. The procedures[31] used were intentionally chosen to minimize defect formation, as defects can alter pore chemistry and pore size, thereby affecting the alane binding capacity and affinity. Following overnight immersion of UiO-67bpy powder in an AlH_3-(*N*,*N*-dimethylethylamine) in toluene solution, a color change from white to dark-purple occurs, changing to brown after drying, as shown in Figure 1a and Figure S1b,c. As a control experiment, we synthesized UiO-67 (see Supporting Information for the MOF synthesis procedure),[26,32] which lacks aromatic chelating nitrogen functionalization. Only a slight color change occurs, from white to gray, when UiO-67 is infiltrated with AlH_3 and dried under vacuum (Figure S1d). This indicates weak interactions, similar to the ones observed in the case of other host materials.[32] Hereafter we focus primarily on UiO-67bpy characterization to gain insight into the AlH_3 behavior within the nitrogen-functionalized framework.

Structural Characterization. Powder X-ray diffraction was collected for as-synthesized samples to confirm the composition. The as-synthesized phases of UiO-67bpy match well the reported crystal structure.[31] Activated phases also maintain their crystallinity compared to the as-synthesized phases, as shown in Figure S2. AlH_3-infiltrated samples maintain crystallinity as compared to the as-synthesized phases (Figure S2), except for slight peak broadening. Attempts to grow single crystals of AlH_3@UiO-67bpy of sufficient quality to allow direct refinements of the Al positions were unsuccessful. In the FTIR spectra, bands characteristic of AlH_3 at around 1650 and 3000 cm^{-1} are clearly visible,[33,34]

https://doi.org/10.1021/jacs.5c15894
J. Am. Chem. Soc. 2025, 147, 47398−47408

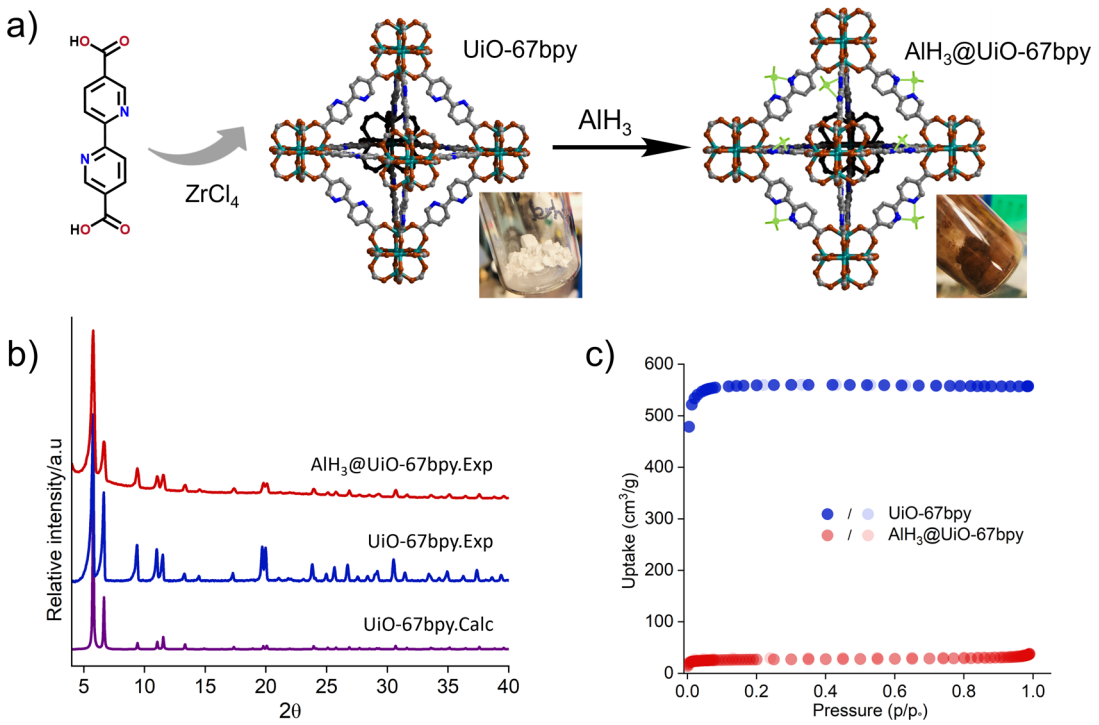

Figure 1. Synthesis and characterization of AlH_3@UiO-67bpy. a) Schematic representation of UiO-67bpy synthesis. Color changes observed upon infiltration with AlH_3 are shown in the top right. b) PXRD of the infiltrated sample compared with the as-synthesized and calculated patterns. c) N_2 adsorption isotherm measured for AlH_3@UiO-67bpy (red) and compared with UiO-67bpy (blue).

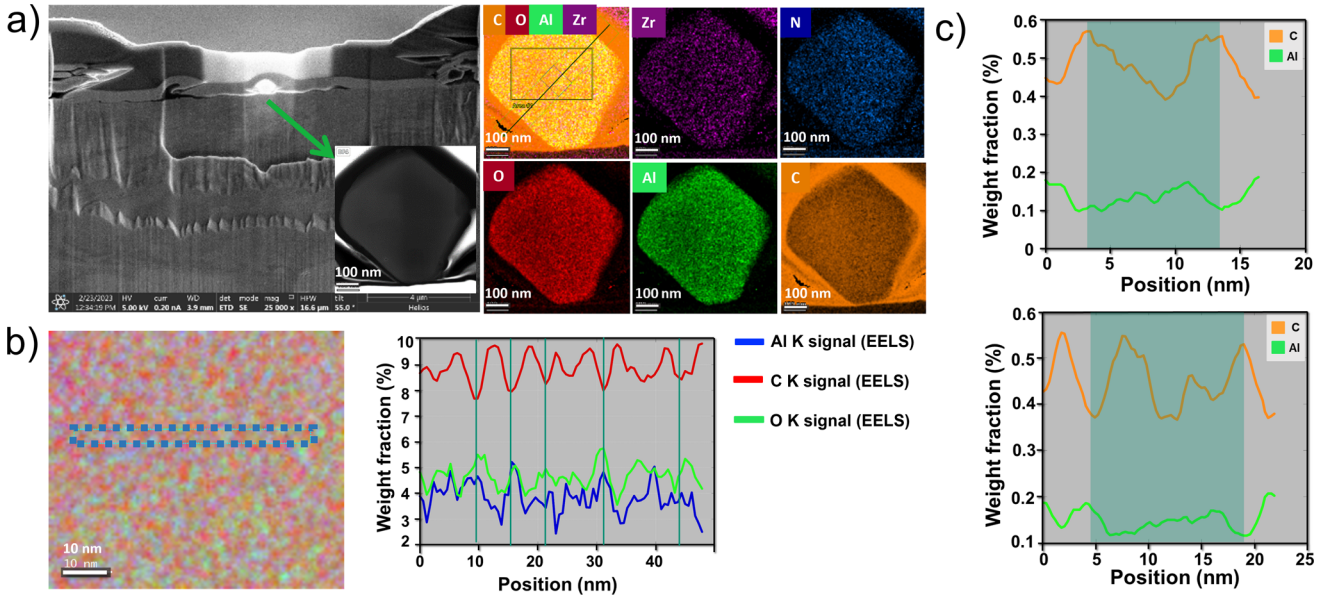

Figure 2. a) TEM and EDX maps of AlH_3@UiO-67bpy show zirconium, nitrogen, oxygen, aluminum, and carbon elemental distributions. The cross-section of the crystal confirms the uniform distribution of aluminum. As shown in the panel, a scanning electron microscopy image of the FIB cross-section with the TEM image in the inset. b) For EELS, the highlighted region was selected to map different signals, including Al (blue), C (red), and O (green). c) Two regions were mapped to correlate Al and C weight fractions, indicating that the peaks for both elements are anticorrelated. This suggests that aluminum is located inside the pore. b,c) The scale bar along the *x*-axis is given in nanometers (nm) and corresponds to the pore diameter of the MOF pore.

although in the infiltrated materials they are broader than those of the pristine hydride, as shown in Figures S3 and S4.

The thermal stability of these materials was tested using thermogravimetric analysis (TGA) (Figure S5). The as-synthesized phase of UiO-67bpy is stable up to 450 °C. A small weight loss at 250 °C corresponds to loss of hydroxyl groups from the zirconium cluster. AlH_3@UiO-67bpy showed a 10% weight loss from 100 to 200 °C, followed by a more gradual weight loss from 350 to 550 °C (Figure S5). Brunauer–Emmett–Teller (BET) surface areas[15] obtained from N_2 sorption isotherms measured at 77 K before and after infiltration (Figure 1c and Figure S6a) indicate a considerable

https://doi.org/10.1021/jacs.5c15894
J. Am. Chem. Soc. 2025, 147, 47398−47408

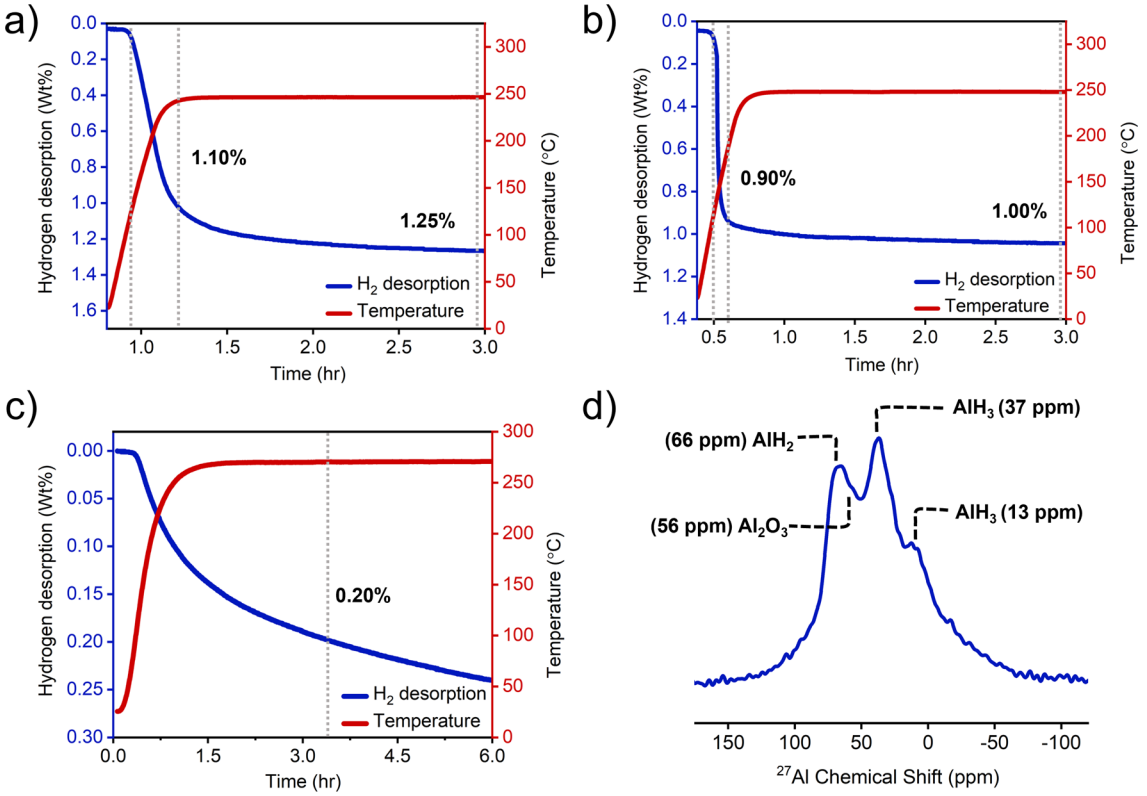

Figure 3. Sieverts measurements for AlH_3@UiO-67bpy first (a) and second cycle (c). Similarly, Sieverts measurements for AlH_3@UiO-67 on the first cycle (b) were conducted to confirm the hydrogen wt % desorption with an increase in temperature. For the second cycle, the rehydrogenation was carried out at 700 bar H_2 and 60 °C. d) MAS NMR measurements were conducted on AlH_3@UiO-67bpy. Three major ^{27}Al signals were found at 13, 37, and 66 ppm for AlH_3, AlH_3, and *AlH_2, respectively. A small peak was found at 56 ppm for Al_2O_3. In a–c), gray dotted vertical lines were used as guides for indicating the extent of H_2 desorption.

reduction in BET surface area and pore volume after AlH_3 loading of UiO-67bpy. The BET surface area (1980 $m^2\ g^{-1}$) and pore volume (0.86 $cm^3\ g^{-1}$) are reduced to 96.16 $m^2\ g^{-1}$ and 0.055 $cm^3\ g^{-1}$, respectively, with similar decreases observed following AlH_3 infiltration in UiO-67 (Figure S6b).

Transmission electron microscopy (TEM) with energy dispersive X-ray (EDX) elemental maps confirm the retention of the characteristic octahedral morphology of UiO-67bpy crystals and the homogeneous distribution of the hydride species. The high-angle annular dark field (HAADF) micrograph shows crystallite in micrometers in size. As shown in Figure S7 on a powder particulate dispersed on a TEM grid, the elemental EDS maps display zirconium, oxygen, carbon, nitrogen, and aluminum. To verify that AlH_3 fully infiltrates the crystal, we performed additional STEM-EDS measurements on a FIB-prepared cross section of a particle. The details of the air-free TEM sample preparation and loading can be found in the SI. For this purpose, we selected smaller crystals of around 100 nm in size to ensure that they were fully infiltrated by the AlH_3 species. STEM-EDS confirms that penetration of AlH_3 species occurs uniformly inside the crystal. The elemental EDS maps are shown individually and overlaid together for zirconium, nitrogen, oxygen, carbon, and aluminum, as shown in Figure 2a. To confirm the location of AlH_3 species, we extracted line profiles from both EDS and measured Electron Energy Loss Spectroscopy (EELS) spectra averaged over several pixels. These reveal that the intensities of carbon from the host network and aluminum are anticorrelated, indicating that Al-containing species are accommodated within the pore (Figure 2b). This confirms that AlH_x species prefer to occupy the pore rather than be randomly distributed on the surface of the host. However, the regular pore structure of UiO-67bpy, with a spacing of 1.5 nm, is altered in the images of the infiltrated sample. The spacing between Al peaks (and between C peaks) in the extracted line profiles is approximately 5 nm and the pores are less regular. This is likely due to damage to the sample caused by the intense electron beam required to obtain high-resolution images and EELS spectra, a phenomenon we previously observed in silver-infiltrated MOFs.[35]

Hydrogen Desorption. Sieverts measurements were conducted to determine the hydrogen desorption capacity and the desorption kinetics as a function of temperature (Figure 3). These results also provide insight into the effects of local environments on nanoconfined AlH_3 within functionalized pores. AlH_3@UiO-67bpy desorbed 1.10 wt % H within 30 min of heating to 250 °C. The temperature was maintained at 250 °C for an additional 2 h, yielding a final desorption capacity of 1.25 wt % H (Figure 3a). This capacity is consistent with the wt % H previously reported for AlH_3@CTF-bpy[21] and corresponds to ∼12.5 wt % AlH_3 loading, equivalent to ∼2.8 AlH_3 molecules per formula unit. Hydrogen desorption from AlH_3@UiO-67 (Figure 3b) yielded 0.90 wt % H desorption within 10 min of heating to 250 °C, with only an additional 0.10% H observed after further heating for 2.5 h at same temperature, resulting in a total desorption of 1.00 wt % H, with an ∼10 wt % AlH_3 loading (∼2.2 molecules per formula unit). This wt % H is comparable to the 1.02 wt % H observed

https://doi.org/10.1021/jacs.5c15894
J. Am. Chem. Soc. 2025, 147, 47398−47408

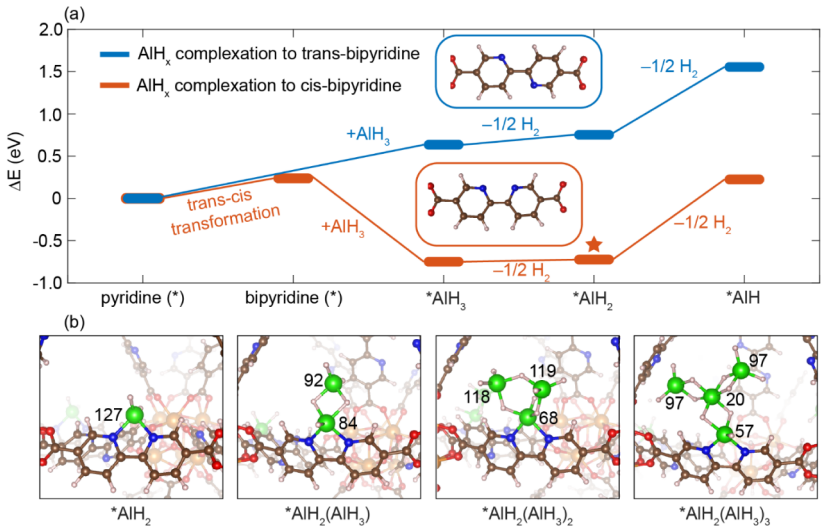

Figure 4. a) DFT-computed potential energy diagrams of AlH_3 complexation to the *trans* and *cis* conformations of bipyridine, and stepwise dehydrogenation. b) DFT-optimized structures of complexed AlH_2 bound by $(AlH_3)_x$ (x = 0−3). Predicted Al chemical shifts of all Al atoms are shown for each structure.

for AlH_3@CTF-biph,[21] indicating that nonfunctionalized frameworks exhibit similar capacities regardless of framework nature or pore size. Hydrogen desorption from AlH_3@UiO-67 is significantly faster than that from AlH_3@UiO-67bpy, revealing a strong AlH_3-bipyridine interaction that stabilizes AlH_3 through coordination to the bpy linkers. Sieverts measurements were also conducted for the pure (non-infiltrated) host frameworks, UiO-67bpy and UiO-67. Both exhibited negligible desorption (0.03 to 0.04 wt % H) upon heating to 270 °C, confirming that AlH_3 is the only source of hydrogen desorption in the AlH_3-infiltrated frameworks (Figure S8).

To probe the reversibility, we exposed the dehydrogenated materials to 700 bar H_2 and 60 °C for 72 h. Sieverts measurements for the resulting samples show that AlH_3@UiO-67bpy desorbed 0.20 wt % H after heating to 270 °C for 3.5 h (Figure 3c). In contrast, AlH_3@UiO-67 showed no reversibility (no hydrogen desorption was observed). The cycling measurements thus reveal that bipyridine functionalization is required to achieve partial reversibility. However, differences in pore volume and pore dimensions may be responsible for the lower capacity and reversibility compared with AlH_3@CTF-bpy (see Discussion section). As additional confirmation of the importance of the bpy functionality for reversible H_2 desorption, we infiltrated cyclam and a G2 PPI dendrimer,[36] two aliphatic compounds that contain tertiary alkyl amines. These compounds form adducts with AlH_3 but the dehydrogenated samples do not exhibit any significant change in the FTIR spectra following treatment with H_2 at 700 bar and 60 °C for 72 h (Figures S9 and S10).

Residual Gas Analysis (RGA) confirmed that the only gas released is H_2 (m/z = 2), demonstrating that the pressure buildup in Sieverts measurements is not associated with impurities or decomposition of the host materials (Figure S11). The crystallinity of the desorbed and rehydrogenated samples was measured and compared with pure host and as-prepared AlH_3 infiltrated samples, as shown in Figure S12. To verify the crystalline stability of the host materials, we also measured *in situ* PXRD between room temperature and 250 °C in intervals of 50 °C (Figure S13). PXRD patterns indicate that MOF crystallinity was maintained and matches the as-prepared samples, except for slight broadening in the low 2θ region. This behavior is consistent with other hydrides confined in Zr-based MOFs, where crystallinity is maintained upon hydrogen release.[29,37]

Magic Angle Spinning NMR Spectroscopy. To gain insight into the coordination environment of AlH_3 within the nitrogen-functionalized pores, we conducted ^{27}Al magic angle spinning nuclear magnetic resonance spectroscopy (MAS NMR). Spectra for the as-prepared AlH_3@UiO-67bpy (Figure 3d) show three major Al chemical environments at 13, 37, and 66 ppm, which suggests several different coordination environments around the Al atoms. However, this behavior is different from previously reported four distinct chemical environments around Al based on our prior work on AlH_3 confinement in CTF-bpy.[21] This indicates that both the pore chemical environment and the pore dimensions affect the Al chemical shifts. A small peak found at 56 ppm may correspond to Al−O species, even though all precautions were taken to avoid oxidation. Importantly, the spectra also show the formation of metallic aluminum peaks at ∼1650 ppm in both AlH_3@UiO-67bpy and AlH_3@UiO-67. After rehydrogenation, the metallic aluminum peak disappears in AlH_3@UiO-67bpy, but is still present in AlH_3@UiO-67. This demonstrates that UiO-67bpy promotes partial reversibility of AlH_3, whereas UiO-67 does not (Figure S14).

DFT Calculations. To gain mechanistic insights from our experimental observations, we employed density functional theory (DFT), *ab initio* molecular dynamics (AIMD), and GIPAW-based chemical shift calculations to probe the electronic and magnetic structure of AlH_3 within UiO-67bpy. We began by determining the preferred location for a molecular unit of AlH_3. Room-temperature AIMD simulations predict that the AlH_3 molecule, initially placed near a zirconium cluster, spontaneously migrates to a bpy-functionalized linker. The lowest-energy configuration of bipyridine in UiO-67bpy is trans (as is the case for molecular bipyridine);[38] consequently, AlH_3 forms a complex with a single nitrogen atom on the linker. In contrast, the AlH_3 molecule diffuses freely and does not stably reside at any location in UiO-67,

https://doi.org/10.1021/jacs.5c15894
J. Am. Chem. Soc. 2025, 147, 47398−47408

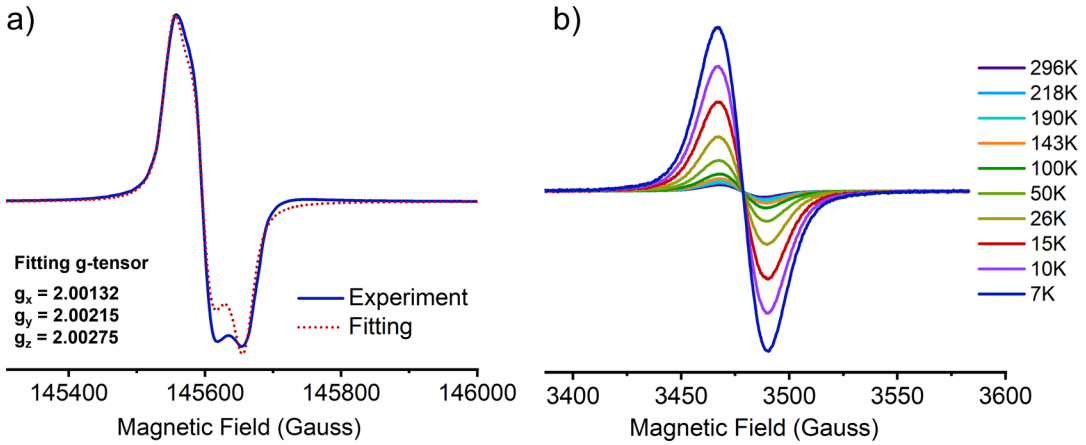

Figure 5. Continuous-wave field-swept EPR spectra of AlH_3@UiO-67bpy at a) 408 GHz and 20 K and b) X-band measurements at 9.74 GHz and variable temperatures.

which lacks nitrogen functionalization. These stronger interactions with bipyridine align with the Sieverts data, which show higher hydrogen capacity for UiO-67bpy compared to UiO-67.

To quantify the stability of AlH_3 complexed with bipyridine, we optimized the AIMD-derived structure and calculated the 0 K reaction energies for AlH_3 complexation, using the DFT energy of bulk AlH_3 as a reference. We also optimized the structures of substoichiometric AlH_3 complexed with bipyridine ($*AlH_2$ and *AlH) and calculated the reaction energies for stepwise dehydrogenation ($*AlH_3 \rightarrow *AlH_2 \rightarrow$ *AlH). As shown in Figure 4a, the complexation of AlH_3 to *trans*-bipyridine in the MOF and the subsequent dehydrogenation steps are all endothermic, indicating that AlH_x complexation with *trans*-bipyridine in UiO-67bpy is unfavorable relative to bulk AlH_3. In prior studies, we observed that *cis*-bipyridine shows a strong affinity for AlH_3 in a triazine covalent framework (CTF). Therefore, we manually altered the bipyridine conformation to explore similar AlH_x interactions with *cis*-bipyridine in UiO-67bpy. Figure 4a illustrates the complete pathway for bipyridine's *trans-to-cis* conformational change, followed by AlH_3 complexation and stepwise dehydrogenation. Although *cis*-bipyridine is slightly less stable than its *trans* conformation, it enables stronger interactions with AlH_x.

The calculations also predict that AlH_3 dissociates upon binding to UiO-67bpy, in which one hydrogen atom spills over to the β-carbon atom of the bpy linker, consistent with previous observations in CTFs.[21] Notably, the formation of $*AlH_2$ (highlighted by the filled star marker) is nearly isoenergetic with $*AlH_3$, indicating a thermodynamic preference for $*AlH_2$ species when entropic contributions are taken into account. The AlH_2-*cis*-bipyridine complex possesses an unpaired electron, making it a radical. Partial charges (computed by using Bader charge analysis) indicate that nearly a full electron ($0.82e^-$) is transferred from AlH_2 to UiO-67bpy, consistent with radical formation. As will be seen below, EPR spectroscopy confirms this prediction.

To further resolve the structures of AlH_3 and AlH_x within UiO-67bpy, we constructed models incorporating additional AlH_3 clusters anchored to $*AlH_2$ and simulated their ^{27}Al chemical shifts. The optimized structures of $*AlH_2(AlH_3)_x$ (x = 1−3) along with the corresponding chemical shifts for each Al atom are shown in Figure 4b. Qualitatively, the model can account for multiple chemical shifts as a result of three different aluminum coordination environments. However, comparisons between absolute values of these shifts may not be justified. For example, although the ^{27}Al chemical shift of $*AlH_2$ is predicted to be 127 ppm in the absence of cluster tethering (consistent with tetrahedrally coordinated aluminum), it does not explain the lack of ^{27}Al peaks above 90 ppm in the experimental spectrum. Anchoring additional AlH_3 units progressively reduces the chemical shift of $*AlH_2$, approaching the 66 ppm peak observed in the ^{27}Al MAS NMR spectrum; we tentatively assign this peak to AlH_2 directly bound to bpy. As the AlH_3 cluster size increases, certain aluminum centers, such as the central Al atom in $*AlH_2(AlH_3)_2$, could adopt octahedral coordination, resulting in even lower chemical shifts. These predictions could explain the peaks at 13 and 37 ppm observed in Figure 3d. Nevertheless, as mentioned above, additional local interactions between aluminum and the MOF pore environment not included in the model could affect the observed NMR spectrum.[39]

Confirmation of Single Electron Transfer. To confirm the DFT prediction of single-electron transfer and formation of AlH_2@UiO-67bpy radicals, we obtained electron paramagnetic resonance (EPR) and UV−visible absorption spectra for the AlH_3-infiltrated MOFs. EPR spectroscopy of AlH_3@UiO-67bpy at 234 and 408 GHz exhibits a large signal from a narrow-line organic radical and rhombic g-anisotropy revealed by the 408 GHz measurements (Figure 5a and Figure S15). As illustrated in Figure S15, at low temperature (20 K), the 408 GHz EPR spectrum clearly shows distinct rhombic g-anisotropy, which progressively diminished at higher temperatures without significant change in overall line width. This is likely due to increased spin−lattice relaxation rates at elevated temperatures.[40] Following AlH_3 nanoconfinement within the UiO-67bpy pores, the EPR response is significantly enhanced relative to the negligible signal detected for the activated UiO-67bpy material (Figure S16). These results are consistent with literature data for similar nanoconfined materials.[41] The observed EPR resonance also exhibits an anisotropic g-tensor (g_x = 2.00132, g_y = 2.00215, g_z = 2.00275), values that are close to previously reported isotropic g-values for AlH_3@CTF-bpy obtained from lower-frequency EPR measurements (g = 2.0032 for AlH_2-bpy[17] and g = 2.0036 for AlH_2@CTF-bpy).[21] The rhombic g-tensor lies in the organic-radical regime typical

https://doi.org/10.1021/jacs.5c15894
J. Am. Chem. Soc. 2025, 147, 47398−47408

for bipyridyl π-radicals, in agreement with the DFT model of AlH_3 to bpy single-electron transfer.

Variable-temperature EPR measurements at X-band (Figure 5b) reveal clear Curie-law behavior ($\chi \propto 1/T$) down to 7 K (Figure S17), confirming isolated paramagnetic radicals without evidence of magnetic ordering or spin fluctuations.[42] Slight deviations from ideal Curie-law behavior observed at higher temperatures may result from weak dipolar interactions among radicals. No resolved hyperfine splitting involving ^{27}Al or ^{1}H nuclei was observed in X-band EPR measurements. This absence of hyperfine structure can be primarily attributed to spin−spin interactions, which broaden EPR spectral lines in densely packed solid-state radicals. These broadening effects typically obscure hyperfine structures that would otherwise be visible under dilute solution conditions.[17]

UV−visible absorption spectra we obtained provide additional evidence of charge transfer upon AlH_3 binding. To support interpretation of these spectra, we performed time-dependent DFT calculations to predict the absorption spectra for *cis*-bpy, AlH_3@*cis*-bpy, AlH_2@*cis*-bpy*, and AlH_2@*cis*-bpy-H (Figure 6). The results indicate that the MOF linker and the

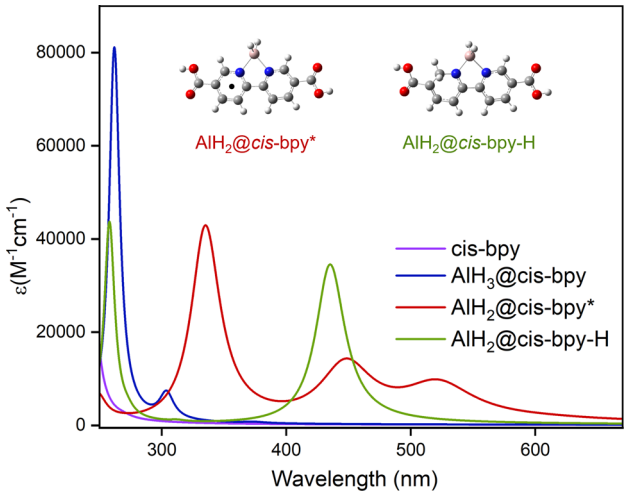

Figure 6. Absorption spectra predicted by TDDFT (ωB97X-D3/def2-TZVPP) (molar extinction coefficient (ε) vs wavelength) of AlH_3@*cis*-bpy, AlH_2@*cis*-bpy, and AlH_2@*cis*-bpy*.

linker bound to AlH_3 should exhibit no absorption in the visible spectrum. However, chemical modifications, such as the removal of a hydrogen atom from AlH_3 to form a radical (AlH_2@*cis*-bpy*), or hydrogenation of the bpy ring with the migrating hydrogen atom (AlH_2@*cis*-bpy-H), result in optically active states within the visible range. Specifically, AlH_2@*cis*-bpy-H is predicted to have an absorption peak around 440 nm, whereas the radical system (AlH_2@*cis*-bpy*) should have peaks at 450 and 520 nm. Although both structures lead to absorption in the visible, the energy of the radical system, plus 1/2 H_2, is predicted to be 0.3 eV lower in energy than the hydrogenated ring configuration. The predicted spectra correspond well with the experimentally observed color change (from white to brown) upon infiltration of UiO-67bpy with AlH_3 and with the corresponding experimental UV−vis spectra (Figure S18).

DISCUSSION

The most important outcome of this research is that it establishes a clear structure−property relationship for thermodynamically stabilizing AlH_3 and, potentially, other metastable hydrides. The combination of coordination to electron-donating aromatic amine functionalities and the steric confinement imposed by the MOF nanopores has several interacting effects. First, both thermodynamic and kinetic stabilization occurs as a result of the Lewis acid−base interaction between the chelating bipyridyl linker groups. The rehydrogenation pressure is reduced by ≈28-fold relative to bulk aluminum and the rate of hydrogen release from AlH_3@UiO-67bpy is significantly slower than from AlH_3@UiO-67 (Figure 3a,b). The mechanism by which this occurs is the remarkable concomitant single-electron transfer of $0.82e^-$ from AlH_2 to bpy by dissociating a hydrogen atom from AlH_3, predicted by DFT calculations (Figure 6) and confirmed by EPR spectroscopy (Figure 5). This chemistry is analogous to reactions in solution between AlH_3 and bipyridine, as observed by Kaim and others.[17] Notably, it is only possible if the amine is chelating, which allows the creation of a stable radical complex.[43] Control experiments using nonchelating, non-aromatic cyclam and dendrimer[36] amines support our overarching hypothesis, as articulated in the Introduction. Moreover, DFT calculations predicted that adding an electron to the bpy linker is energetically more favorable than to cyclam, which indicates that the free radical is stabilized in the aromatic linker but not in the aliphatic groups (Table S1).

The chelating requirement has implications for the method of UiO-67bpy synthesis. In solution, the stable linker isomer is *trans*-$bpydc^{2-}$, which binds AlH_3 more weakly than the *cis* linker. The barrier to *trans*−*cis* isomerization within the framework is too large (0.62 eV) to be thermally overcome. However, prior investigations indicate that acidic synthesis conditions can promote rotation by protonating *trans*-$bpydc^{2-}$.[38,44] DFT calculations (Figure S19) show that even under neutral synthesis conditions the barrier is reduced to 0.36 eV relative to rotation within the MOF, while acidic conditions reduce it to 0.22 eV. Consequently, slightly acidic conditions used during MOF synthesis could promote *trans*- to *cis*- rotation.

In our previous work we demonstrated that $Mg(BH_4)_2$ could be incorporated into UiO-67bpy, but there was no obvious sign of a radical being formed.[26] Magnesium exists as a Mg^{2+} ion fully coordinated by stable BH_4^- anions, leading to primarily ionic interactions without electron transfer to the host. The ^{27}Al MAS NMR shows the presence of a small shoulder around 56 ppm, which may indicate the presence of some Al−O species. Nevertheless, the data support the notion that most of the Al exists in the form of a hydride, which is also supported by Sieverts measurements. Consequently, the origin of this difference is not clear but suggests that, beyond the selection of the framework itself, the chemical reactivity and affinity of the guest species toward the host matrix are critical factors influencing stability and charge transfer. Moreover, the propensity for oxidation likely depends on the intrinsic properties and functionalization of the encapsulated hydride.[19,45] Careful selection of both the hydride guest and the host framework are therefore essential for designing effective nanoscaling strategies that can enhance material performance.[15]

https://doi.org/10.1021/jacs.5c15894
J. Am. Chem. Soc. 2025, 147, 47398−47408

A second effect is that nanoconfinement inhibits the formation of large aluminum clusters that could further agglomerate. Although spatial limitations of this nature are often cited as a motivation for nanoscaling, in this case they are critical for achieving reversible hydrogen desorption. Our results for AlH_3@UiO-67bpy and AlH_3@CTF-bpy suggest that, as Al_xH_y clusters increase in size, their properties approach those of the bulk material. The consequent lower thermodynamic stability leads to hydrogen release and formation of metallic aluminum that cannot be rehydrogenated. Supporting this concept are the Sieverts data (Figure 3a,b) and corresponding ^{27}Al NMR spectra for AlH_3@UiO-67bpy (Figure 3d and Figure S14), which show that Al(0) that formed during the initial H_2 release disappears upon re-exposure to H_2. In contrast, a large Al(0) peak in the ^{27}Al NMR spectrum of desorbed AlH_3@CTF-bpy does not disappear upon rehydrogenation. This suggests that AlH_3@CTF-bpy contains substantial amounts of AlH_3 that is not coordinated to bpy and is thus free to form large clusters or nanoparticles that decompose upon heating to form bulk Al.[21] Although additional data across a range of framework functionalities and pore dimensions will be needed for quantitative conclusions, it is evident that UiO-67bpy effectively prevents agglomeration, whereas CTF-bpy does not.[21] Moreover, nanoconfinement influences the thermal stability of the hydride@MOF composite (Figure S5), suggesting that, in principle, a mixed-linker strategy could be employed to both enhance framework stability and thermodynamically stabilize alane.

The ^{27}Al NMR spectra and DFT calculations reveal a third possible structure−property relationship: namely, that by binding multiple AlH_3 molecules to a single bpy linker the volumetric storage capacity can be several times greater than predicted from monomolecular chemisorption. The DFT-predicted chemical shifts suggest that these clusters could be as large as $(AlH_3)_7$ and still fit into the MOF pores. Three distinct aluminum coordination environments are evident (Figure 3d), which may correspond to different Al−H species based on our DFT-predicted chemical shifts.[21] A prior assessment of design strategies for increasing the ambient-temperature capacity of adsorbents indicated that strong binding sites capable of coordinating multiple H_2 molecules would be necessary to meet the DOE technical targets for light-duty vehicles.[1,46] Long and coworkers successfully demonstrated both strong binding sites[47] and multiple H_2 binding[48] in separate MOFs, but combining the two within a single structure has not been demonstrated. The properties of AlH_3@UiO-67bpy and AlH_3@CTF-bpy indicate this is possible by chemisorption on Al clusters rather than H_2 physisorption to MOF open metal sites.[41]

We note that although AlH_3@UiO-67bpy has somewhat lower gravimetric hydrogen capacity than our previously reported AlH_3@CTF-bpy,[21] the results presented here demonstrate that CTF-bpy is not unique in its ability to stabilize AlH_3, and possibly other metastable hydrides. This has considerable significance because it suggests that this hydride, comprised of earth-abundant aluminum, could overcome critical problems limiting the use of other main group hydrides. Specifically, rehydrogenation is possible under much milder thermal conditions than most complex metal hydrides.[49] Moreover, there are no kinetic sinks in the reaction chemistry that block reversibility, as is the case for borohydrides.[50] Although we were not able to measure the equilibrium thermodynamic properties, it is likely that H_2 release from both AlH_3@CTF-bpy[21] and AlH_3@UiO-67bpy is only slightly endothermic, which is advantageous for storage applications where a high hydrogen delivery rate is required.[1]

CONCLUSIONS

To understand how host−guest interactions govern nanoconfinement of metastable metal hydrides, we used the crystalline Zr-MOFs UiO-67 and UiO-67bpy as a model platform for incorporating AlH_3. Both UiO-67 and UiO-67bpy retain crystallinity upon AlH_3 loading and subsequent hydrogen cycling. The transmission electron microscopy (TEM) using Focused Ion Beam (FIB) sample preparation reveals that aluminum-containing species are distributed uniformly throughout the MOF crystals. Hydrogen release and uptake measurements showed that AlH_3@UiO-67bpy displays partial reversibility, whereas no reversibility was observed for AlH_3@UiO-67, a behavior consistent with that previously reported for AlH_3@CTF-biph versus AlH_3@CTF-bpy.[21] EPR data, UV-visible absorption spectra, and DFT calculations further indicate that UiO-67bpy promotes a single-electron transfer mechanism, facilitating hydride binding and generating an organic radical with a Curie-law behavior ($\chi \propto 1/T$) from RT down to 7 K. This mechanism aligns with earlier work on AlH_3@CTF-bpy,[21] which benefits from a larger pore size and extended aromatic host structure. Together, these results highlight the role of host functionality and pore size in controlling the AlH_3 cluster size and environments, providing molecular-level design principles for tailoring suitable hosts for thermodynamic stabilization of metastable metal hydrides.

Beyond this specific system, our recent application of a codesign strategy[51] shows that nanoscaling does not necessarily reduce storage capacity. Rather, synergies between the nanohydride and its host can improve not only thermodynamics, but in selected cases can even increase usable hydrogen capacity relative to the bulk material. The nanoconfinement strategy also opens new opportunities to probe the chemical environments of other metal hydrides by selecting suitable porous hosts.[15,28] It could also be powerful to use the Crystalline Sponge Method, introduced by Fujita,[52] to incorporate metal hydride clusters within a periodic framework to allow detailed structure determinations by X-ray, neutron, or electron diffraction. A wide array of crystalline MOF hosts are available[53] to confine such hydride clusters and enable precise determination of their size and coordination environment. These conclusions strongly motivate additional research, driven by the need for economically viable hydrogen storage and by the potential of hydrogen as an energy vector with gravimetric capacity exceeding that of lithium ion batteries.[54] Although 700 bar is indeed a high pressure, nevertheless it is well within the practical range of current hydrogen compression technologies[55] (both conventional and metal hydride-based) and is used in the current generation of hydrogen fuel cell vehicles. Importantly, our mechanistic findings establish critical structure−property relationships that underpin material stabilization through nanoconfinement. They also suggest strategies for tuning the outcome of chemical reactions[56] and expanding the thermodynamic limits of metastability.[57]

https://doi.org/10.1021/jacs.5c15894
J. Am. Chem. Soc. 2025, 147, 47398−47408

■ ASSOCIATED CONTENT

Supporting Information

The Supporting Information is available free of charge at https://pubs.acs.org/doi/10.1021/jacs.5c15894.

Additional experimental details, including crystallographic and powder sample images, thermal measurements, gas sorption measurements, TEM measurements, Seiverts measurements for host frameworks, alane infiltration in cyclam and dendrimer, UV−vis measurements, *ab initio* calculations and computational spectroscopy, TGA, RGA, FTIR, NMR, EPR, and XRD data (PDF)

■ AUTHOR INFORMATION

Corresponding Authors

Mark D. Allendorf − *Sandia National Laboratories, Livermore, California 94550, United States; Department of Chemistry, Washington University in St. Louis, St. Louis, Missouri 63130, United States;* orcid.org/0000-0001-5645-8246; Email: mdallendorf@wustl.edu

Vitalie Stavila − *Sandia National Laboratories, Livermore, California 94550, United States;* orcid.org/0000-0003-0981-0432; Email: vnstavi@sandia.gov

Authors

Mohana Shivanna − *Sandia National Laboratories, Livermore, California 94550, United States;* orcid.org/0000-0002-8933-305X

Nicole A. Torquato − *Sandia National Laboratories, Livermore, California 94550, United States*

Sichi Li − *Lawrence Livermore National Laboratory, Livermore, California 94550, United States;* orcid.org/0000-0002-2565-5906

Maxwell A. T. Marple − *Lawrence Livermore National Laboratory, Livermore, California 94550, United States;* orcid.org/0000-0001-5251-8301

Joshua D. Sugar − *Sandia National Laboratories, Livermore, California 94550, United States*

Michael E. Foster − *Sandia National Laboratories, Livermore, California 94550, United States;* orcid.org/0000-0002-4164-3526

Ashlynn Berry − *Department of Chemistry, Washington University in St. Louis, St. Louis, Missouri 63130, United States;* orcid.org/0000-0002-0257-4732

William V. Taylor − *Sandia National Laboratories, Livermore, California 94550, United States*

Nicholas A. Strange − *SLAC National Accelerator Laboratory, Menlo Park, California 94025, United States;* orcid.org/0000-0001-5699-7274

Xiaoling Wang − *California State University East Bay, Hayward, California 94542, United States*

Farid El Gabaly − *Sandia National Laboratories, Livermore, California 94550, United States;* orcid.org/0000-0002-5822-9938

Tieyan Chang − *NSF's ChemMatCARS, University of Chicago, Chicago, Illinois 60637, United States;* orcid.org/0000-0002-7434-3714

Yu Sheng Chen − *NSF's ChemMatCARS, University of Chicago, Chicago, Illinois 60637, United States*

Peter A. Sharma − *Sandia National Laboratories, Albuquerque, New Mexico 87185, United States;* orcid.org/0000-0002-3071-7382

John Lemmon − *Breakthrough Energy Fellows, Richland, Washington 99352, United States*

Bryce Sadtler − *Department of Chemistry, Washington University in St. Louis, St. Louis, Missouri 63130, United States;* orcid.org/0000-0003-4860-501X

Brandon C. Wood − *Lawrence Livermore National Laboratory, Livermore, California 94550, United States*

Complete contact information is available at: https://pubs.acs.org/10.1021/jacs.5c15894

Author Contributions

The manuscript was written through contributions of all authors. All authors have given their approval to the final version of the manuscript.

Notes

The authors declare no competing financial interest.

■ ACKNOWLEDGMENTS

The authors thank Brendan Davis and Robert Horton for their technical assistance with the hydrogen uptake and release experiments. We thank Prof. Bettina V. Lotsch and Dr. Xue Wang at Ludwig Maximilian University of Munich for providing samples of CTFs and for their technical insights. Sandia National Laboratories is a multimission laboratory managed and operated by National Technology & Engineering Solutions of Sandia, LLC (NTESS), a wholly owned subsidiary of Honeywell International Inc., for the U.S. Department of Energy's National Nuclear Security Administration (DOE/NNSA) under contract DE-NA0003525. The computational portion of the work was performed under the auspices of the DOE by Lawrence Livermore National Laboratory (LLNL) under contract DE-AC52-07NA27344 using computational resources sponsored by the DOE's EERE and located at the National Renewable Energy Laboratory. EPR experiments were performed at the National High Magnetic Field Laboratory (NHMFL), which is supported by National Science Foundation Cooperative Agreement no. DMR-2128556, and with the support of the grant NSF CHE-2320338 and the State of Florida. The authors would like to thank Andrzej Ozarowski (NHMFL), Tomas Orlando (NHMFL), and Anthony Xu Peng Ma (CSUEB) for their help with EPR data collection. X.W. acknowledges the support of the U.S. Department of Energy, Office of Science, Office of Basic Energy Sciences, under Award DE-SC0025712. The authors acknowledge funding from the U.S. Department of Energy, Office of Energy Efficiency and Renewable Energy, Fuel Cell Technologies Office, through the Hydrogen Storage Materials Advanced Research Consortium (HyMARC). A.B. was supported by the U.S. Department of Energy, Office of Science, Office of Workforce Development for Teachers and Scientists, Office of Science Graduate Student Research (SCGSR) program. The SCGSR program is administered by the Oak Ridge Institute for Science and Education for the DOE under contract number DE-SC0014664. This work was also supported by the Sandia Laboratory Directed Research and Development (LDRD) Program and by a Breakthrough Energy Explorer Grant. Y.-S.C. and T.C. would like to thank ChemMatCARS, Sector 15 at the Advanced Photon Source (APS), Argonne National Laboratory (ANL), is supported by the Divisions of Chemistry (CHE) and Materials Research (DMR), National Science Foundation, under grant numbers NSF/CHE-1834750 and NSF/CHE- 2335833.

REFERENCES

(1) Allendorf, M. D.; Stavila, V.; Snider, J. L.; Witman, M.; Bowden, M. E.; Brooks, K.; Tran, B. L.; Autrey, T. Challenges to developing materials for the transport and storage of hydrogen. *Nat. Chem.* **2022**, *14*, 1214−1223.

(2) Graetz, J.; Vajo, J. J. Controlled hydrogen release from metastable hydrides. *J. Alloys Compd.* **2018**, *743*, 691−696.

(3) Wehmschulte, R. J.; Power, P. P. Primary alanes and alanates: useful synthetic reagents in aluminum chemistry. *Polyhedron* **2000**, *19*, 1649−1661.

(4) Shivanna, M.; Elmslie, T. A.; Spataru, C. D.; Duwal, S.; Porcellino, N.; Mouzaya, S.; Pakhanyan, C. P.; El Gabaly, F.; Kawaguchi-Imada, S.; Guo, J.; Zhuo, Z.; Kim, M.-J.; Sturtevant, B. T.; Teprovich, J. A.; Allendorf, M. D.; Sharma, P. A.; Stavila, V. Nanoconfinement of High Hydrogen-to-Metal Ratio Lanthanum Hydrides in Functionalized Carbon Hosts. *ACS Appl. Energy Mater.* **2025**, *8*, 7−15.

(5) Graetz, J.; Hauback, B. C. Recent developments in aluminum-based hydrides for hydrogen storage. *MRS Bull.* **2013**, *38*, 473−479.

(6) Grew, K. N.; Brownlee, Z. B.; Shukla, K. C.; Chu, D. Assessment of Alane as a hydrogen storage media for portable fuel cell power sources. *J. Power Sources* **2012**, *217*, 417−430.

(7) Trowell, K. A.; Goroshin, S.; Frost, D. L.; Bergthorson, J. M. Aluminum and its role as a recyclable, sustainable carrier of renewable energy. *Appl. Energy* **2020**, *275*, 115112.

(8) Brower, F. M.; Matzek, N. E.; Reigler, P. F.; Rinn, H. W.; Roberts, C. B.; Schmidt, D. L.; Snover, J. A.; Terada, K. Preparation and properties of aluminum hydride. *J. Am. Chem. Soc.* **1976**, *98*, 2450−2453.

(9) Graetz, J.; Reilly, J. J.; Yartys, V. A.; Maehlen, J. P.; Bulychev, B. M.; Antonov, V. E.; Tarasov, B. P.; Gabis, I. E. Aluminum hydride as a hydrogen and energy storage material: Past, present and future. *J. Alloys Compd.* **2011**, *509*, S517−S528.

(10) Graetz, J.; Reilly, J. J. Thermodynamics of the α,β and γ polymorphs of AlH3. *J. Alloys Compd.* **2006**, *424*, 262−265.

(11) Orimo, S.; Nakamori, Y.; Kato, T.; Brown, C.; Jensen, C. M. Intrinsic and mechanically modified thermal stabilities of α-, β- and γ-aluminum trihydrides AlH3. *Appl. Phys. A.* **2006**, *83*, 5−8.

(12) Konovalov, S. K.; Bulychev, B. M. The P,T-State Diagram and Solid Phase Synthesis of Aluminum Hydride. *Inorg. Chem.* **1995**, *34*, 172−175.

(13) Martínez-Rodríguez, M. J.; García-Díaz, B. L.; Teprovich, J. A.; Knight, D. A.; Zidan, R. Advances in the electrochemical regeneration of aluminum hydride. *Appl. Phys. A.* **2012**, *106*, 545−550.

(14) Wong, B. M.; Lacina, D.; Nielsen, I. M. B.; Graetz, J.; Allendorf, M. D. Thermochemistry of Alane Complexes for Hydrogen Storage: A Theoretical and Experimental Investigation. *J. Phys. Chem. C* **2011**, *115*, 7778−7786.

(15) Schneemann, A.; White, J. L.; Kang, S.; Jeong, S.; Wan, L. F.; Cho, E. S.; Heo, T. W.; Prendergast, D.; Urban, J. J.; Wood, B. C.; Allendorf, M. D.; Stavila, V. Nanostructured metal hydrides for hydrogen storage. *Chem. Rev.* **2018**, *118*, 10775−10839.

(16) Cho, Y.; Cho, H.; Cho, E. S. Nanointerface Engineering of Metal Hydrides for Advanced Hydrogen Storage. *Chem. Mater.* **2023**, *35*, 366−385.

(17) Kaim, W. Single electron transfer reaction of aluminum hydride with nitrogen-containing heterocycles. ESR characterization of the radical products. *J. Am. Chem. Soc.* **1984**, *106*, 1712−1716.

(18) Graetz, J.; Chaudhuri, S.; Wegrzyn, J.; Celebi, Y.; Johnson, J. R.; Zhou, W.; Reilly, J. J. Direct and Reversible Synthesis of AlH3−Triethylenediamine from Al and H2. *J. Phys. Chem. C* **2007**, *111*, 19148−19152.

(19) Cho, Y.; Li, S.; Snider, J. L.; Marple, M. A. T.; Strange, N. A.; Sugar, J. D.; El Gabaly, F.; Schneemann, A.; Kang, S.; Kang, M.-H.; Park, H.; Park, J.; Wan, L. F.; Mason, H. E.; Allendorf, M. D.; Wood, B. C.; Cho, E. S.; Stavila, V. Reversing the Irreversible: Thermodynamic Stabilization of LiAlH4 Nanoconfined Within a Nitrogen-Doped Carbon Host. *ACS Nano* **2021**, *15*, 10163−10174.

(20) Pratthana, C.; Yang, Y.; Rawal, A.; Aguey-Zinsou, K.-F. Nanoconfinement of lithium Alanate for hydrogen storage. *J. Alloys Compd.* **2022**, *926*, 166834.

(21) Stavila, V.; Li, S.; Dun, C.; Marple, M. A. T.; Mason, H. E.; Snider, J. L.; Reynolds, J. E., III; El Gabaly, F.; Sugar, J. D.; Spataru, C. D.; et al. Defying Thermodynamics: Stabilization of Alane Within Covalent Triazine Frameworks for Reversible Hydrogen Storage. *Angew. Chem., Int. Ed.* **2021**, *60*, 25815−25824.

(22) Furukawa, H.; Cordova, K. E.; O'Keeffe, M.; Yaghi, O. M. The Chemistry and Applications of Metal-Organic Frameworks. *Science* **2013**, *341*, 1230444.

(23) Zhou, H.-C. J.; Kitagawa, S. Metal−Organic Frameworks (MOFs). *Chem. Soc. Rev.* **2014**, *43*, 5415−5418.

(24) Stavila, V.; Bhakta, R. K.; Alam, T. M.; Majzoub, E. H.; Allendorf, M. D. Reversible Hydrogen Storage by NaAlH4 Confined within a Titanium-Functionalized MOF-74(Mg) Nanoreactor. *ACS Nano* **2012**, *6*, 9807−9817.

(25) Bhakta, R. K.; Herberg, J. L.; Jacobs, B.; Highley, A.; Behrens, R.; Ockwig, N. W.; Greathouse, J. A.; Allendorf, M. D. Metal−Organic Frameworks As Templates for Nanoscale NaAlH4. *J. Am. Chem. Soc.* **2009**, *131*, 13198−13199.

(26) Schneemann, A.; Wan, L. F.; Lipton, A. S.; Liu, Y.-S.; Snider, J. L.; Baker, A. A.; Sugar, J. D.; Spataru, C. D.; Guo, J.; Autrey, T. S.; Jørgensen, M.; Jensen, T. R.; Wood, B. C.; Allendorf, M. D.; Stavila, V. Nanoconfinement of Molecular Magnesium Borohydride Captured in a Bipyridine-Functionalized Metal−Organic Framework. *ACS Nano* **2020**, *14*, 10294−10304.

(27) Callini, E.; Szilágyi, P. Á.; Paskevicius, M.; Stadie, N. P.; Réhault, J.; Buckley, C. E.; Borgschulte, A.; Züttel, A. Stabilization of volatile Ti(BH4)3 by nano-confinement in a metal−organic framework. *Chem. Sci.* **2016**, *7*, 666−672.

(28) Wang, Y.; Xue, Y.; Züttel, A. Nanoscale engineering of solid-state materials for boosting hydrogen storage. *Chem. Soc. Rev.* **2024**, *53*, 972−1003.

(29) Provinciali, G.; Consoli, N. A.; Caliandro, R.; Mangini, V.; Barba, L.; Giannini, C.; Tuci, G.; Giambastiani, G.; Lelli, M.; Rossin, A. Ammonia Borane and Hydrazine Bis(borane) Confined within Zirconium Bithiazole and Bipyridyl Metal−Organic Frameworks as Chemical Hydrogen Storage Materials. *J. Phys. Chem. C* **2025**, *129*, 6094−6108.

(30) Rossin, A.; Tuci, G.; Luconi, L.; Giambastiani, G. Metal−Organic Frameworks as Heterogeneous Catalysts in Hydrogen Production from Lightweight Inorganic Hydrides. *ACS Catal.* **2017**, *7*, 5035−5045.

(31) Gonzalez, M. I.; Bloch, E. D.; Mason, J. A.; Teat, S. J.; Long, J. R. Single-crystal-to-single-crystal metalation of a metal-organic framework: a route toward structurally well-defined catalysts. *Inorg. Chem.* **2015**, *54*, 2995−3005.

(32) Fei, H.; Cohen, S. M. A robust, catalytic metal−organic framework with open 2,2′-bipyridine sites. *Chem. Commun.* **2014**, *50*, 4810−4812.

(33) Chertihin, G. V.; Andrews, L. Reactions of pulsed-laser ablated aluminum atoms with hydrogen: infrared spectra of aluminum hydride (AlH, AlH2, AlH3, and Al2H2) species. *J. Phys. Chem.* **1993**, *97*, 10295−10300.

(34) Wang, X.; Andrews, L.; Tam, S.; DeRose, M. E.; Fajardo, M. E. Infrared Spectra of Aluminum Hydrides in Solid Hydrogen: Al2H4 and Al2H6. *J. Am. Chem. Soc.* **2003**, *125*, 9218−9228.

(35) Houk, R. J. T.; Jacobs, B. W.; Gabaly, F. E.; Chang, N. N.; Talin, A. A.; Graham, D. D.; House, S. D.; Robertson, I. M.; Allendorf, M. D. Silver Cluster Formation, Dynamics, and Chemistry in Metal−Organic Frameworks. *Nano Lett.* **2009**, *9*, 3413−3418.

(36) Tack, F.; Bakker, A.; Maes, S.; Dekeyser, N.; Bruining, M.; Elissen-Roman, C.; Janicot, M.; Janssen, H. M.; De Waal, B. F. M.; Fransen, P. M. Dendrimeric poly(propylene-imines) as effective delivery agents for DNAzymes: Dendrimer synthesis, stability and oligonucleotide complexation. *J. Controlled Release* **2006**, *116*, e24−e26.

https://doi.org/10.1021/jacs.5c15894
J. Am. Chem. Soc. 2025, 147, 47398−47408

(37) Chung, J.-Y.; Liao, C.-W.; Chang, Y.-W.; Chang, B. K.; Wang, H.; Li, J.; Wang, C.-Y. Influence of Metal−Organic Framework Porosity on Hydrogen Generation from Nanoconfined Ammonia Borane. *J. Phys. Chem. C* **2017**, *121*, 27369−27378.
(38) Howard, S. T. Conformers, Energetics, and Basicity of 2,2'-Bipyridine. *J. Am. Chem. Soc.* **1996**, *118*, 10269−10274.
(39) Lucier, B. E. G.; Chen, S.; Huang, Y. Characterization of Metal−Organic Frameworks: Unlocking the Potential of Solid-State NMR. *Acc. Chem. Res.* **2018**, *51*, 319−330.
(40) Weil, J. A.; Bolton James, R. *Electron Paramagnetic Resonance: elementary Theory and Practical Applications*; Wiley, 2007.
(41) Faust, T. B.; D'Alessandro, D. M. Radicals in metal−organic frameworks. *RSC Adv.* **2014**, *4*, 17498−17512.
(42) Ndamyabera, C. A.; Langmi, H. W. Recent Developments in Organic Radical Inclusion in MOFs and Radical MOFs. *ChemistryOpen* **2025**, *14*, e2500069.
(43) Kaim, W. Aluminiumorganische radikalkomplexe von N-heterozyklen: I. Pyridin-derivate. *J. Organomet. Chem.* **1981**, *215*, 325−335.
(44) Nakamoto, K. Ultraviolet Spectra and Structures of 2,2'-Bipyridine and 2,2',2″-Terpyridine in Aquous Solution. *J. Phys. Chem.* **1960**, *64*, 1420−1425.
(45) Wood, B. C.; Heo, T. W.; Kang, S.; Wan, L. F.; Li, S. Beyond idealized models of nanoscale metal hydrides for hydrogen storage. *Ind. Eng. Chem. Res.* **2020**, *59*, 5786−5796.
(46) Allendorf, M. D.; Hulvey, Z.; Gennett, T.; Ahmed, A.; Autrey, T.; Camp, J.; Seon Cho, E.; Furukawa, H.; Haranczyk, M.; Head-Gordon, M.; Jeong, S.; Karkamkar, A.; Liu, D.-J.; Long, J. R.; Meihaus, K. R.; Nayyar, I. H.; Nazarov, R.; Siegel, D. J.; Stavila, V.; Urban, J. J.; Veccham, S. P.; Wood, B. C. An assessment of strategies for the development of solid-state adsorbents for vehicular hydrogen storage. *Energy Environ. Sci.* **2018**, *11*, 2784−2812.
(47) Jaramillo, D. E.; Jiang, H. Z. H.; Evans, H. A.; Chakraborty, R.; Furukawa, H.; Brown, C. M.; Head-Gordon, M.; Long, J. R. Ambient-Temperature Hydrogen Storage via Vanadium(II)-Dihydrogen Complexation in a Metal−Organic Framework. *J. Am. Chem. Soc.* **2021**, *143*, 6248−6256.
(48) Dincă, M.; Long, J. R. Hydrogen Storage in Microporous Metal−Organic Frameworks with Exposed Metal Sites. *Angew. Chem., Int. Ed.* **2008**, *47*, 6766−6779.
(49) Dematteis, E. M.; Amdisen, M. B.; Autrey, T.; Barale, J.; Bowden, M. E.; Buckley, C. E.; Cho, Y. W.; Deledda, S.; Dornheim, M.; de Jongh, P.; Grinderslev, J. B.; Gizer, G.; Gulino, V.; Hauback, B. C.; Heere, M.; Heo, T. W.; Humphries, T. D.; Jensen, T. R.; Kang, S. Y.; Lee, Y.-S.; Li, H.-W.; Li, S.; Møller, K. T.; Ngene, P.; Orimo, S.-I.; Paskevicius, M.; Polanski, M.; Takagi, S.; Wan, L.; Wood, B. C.; Hirscher, M.; Baricco, M. Hydrogen storage in complex hydrides: past activities and new trends. *Prog. Energy* **2022**, *4*, 032009.
(50) Liu, J.; Ma, Y.; Yang, J.; Sun, L.; Guo, D.; Xiao, P. Recent advance of metal borohydrides for hydrogen storage. *Front. Chem.* **2022**, *10*, 945208.
(51) Witman, M. D.; Brooks, K. P.; Sprik, S. J.; Wood, B. C.; Heo, T. W.; Ray, K. G.; Klebanoff, L. E.; Acosta, A.; Stavila, V.; Allendorf, M. D. A Bulk versus Nanoscale Hydrogen Storage Paradox Revealed by Material-System Co-Design. *Adv. Funct. Mater.* **2024**, *34*, 2411763.
(52) Inokuma, Y.; Yoshioka, S.; Ariyoshi, J.; Arai, T.; Hitora, Y.; Takada, K.; Matsunaga, S.; Rissanen, K.; Fujita, M. X-ray analysis on the nanogram to microgram scale using porous complexes. *Nature* **2013**, *495*, 461−466.
(53) Zigon, N.; Duplan, V.; Wada, N.; Fujita, M. Crystalline Sponge Method: X-ray Structure Analysis of Small Molecules by Post-Orientation within Porous Crystals-Principle and Proof-of-Concept Studies. *Angew. Chem., Int. Ed.* **2021**, *60*, 25204−25222.
(54) Wang, X.; Peng, P.; Witman, M. D.; Stavila, V.; Allendorf, M. D.; Breunig, H. M. Technoeconomic Insights into Metal Hydrides for Stationary Hydrogen Storage. *Adv. Sci.* **2025**, *12*, 2415736.
(55) Lototskyy, M. V.; Yartys, V. A.; Pollet, B. G.; Bowman, R. C. Metal hydride hydrogen compressors: A review. *Int. J. Hydrog. Energy* **2014**, *39*, 5818−5851.
(56) Grommet, A. B.; Feller, M.; Klajn, R. Chemistry under nanoconfinement. *Nat. Nanotechnol.* **2020**, *15*, 256−271.
(57) Sun, W.; Dacek, S. T.; Ong, S. P.; Hautier, G.; Jain, A.; Richards, W. D.; Gamst, A. C.; Persson, K. A.; Ceder, G. The thermodynamic scale of inorganic crystalline metastability. *Sci. Adv.* **2016**, *2*, e1600225.

https://doi.org/10.1021/jacs.5c15894
J. Am. Chem. Soc. 2025, 147, 47398−47408